OPTICAL INVESTIGATION OF TURBULENCE MODULATION IN AN EXTERNALLY FORCED, HIGH REYNOLDS NUMBER BOUNDARY LAYER

Matthew R. Kemnetz

Department of Aerospace and Mechanical Engineering
University of Notre Dame
Notre Dame, Indiana, 46556
mkemnetz@nd.edu

Stanislav Gordeyev

Department of Aerospace and Mechanical Engineering
University of Notre Dame
Notre Dame, Indiana, 46556
sgordeye@nd.edu

Piyush Ranade

Department of Advanced Technology
Honeywell Aerospace
1985 Douglas Drive N, Golden Valley, Minnesota, 55422
piyush.ranade@honeywell.com

Eric J. Jumper

Department of Aerospace and Mechanical Engineering
University of Notre Dame
Notre Dame, Indiana, 46556
jumper.1@nd.edu

ABSTRACT

An optical investigation of an externally forced boundary layer is presented. Measurements were conducted in Notre Dame's Compressible Shear Layer Facility. The forced shear layer created an organized spatially-temporally-varying external flow outside the boundary layer. Full phase-locked 2D optical wavefronts were taken and compared with the previously-collected phase-locked velocity data. Local increase in temporal variance of the wavefronts was found to be associated with a local increase in turbulence intensity due to turbulence amplification events inside the boundary layer. Discrepancies between the amplitudes of optical distortions, experimentally measured and predicted using the Strong Reynolds Analogy, indicated that the pressure fluctuations inside the turbulence amplified regions are not negligible and contribute to the optical distortions. An updated model with included pressure-related terms is derived and it was shown to correctly predict experimental optical results.

INTRODUCTION

Turbulent amplification or modulation in turbulent boundary layers has been studied since the 1960s (Kline *et al.*, 1967). Due to recent advances in experimental techniques, significant progress has been made in the study of the flow physics related to the turbulence modulation or amplification in the near wall region. This turbulent amplification phenomenon has traditionally been studied in a canonical zero pressure-gradient turbulent boundary layer by observing the interactions between the large scales in the outer boundary layer and the small scales in the inner layer. More recently, researchers have begun to study this interaction between the large and small scales by exciting synthetic large scales inside the boundary layer through dynamic roughness excitation. This experimental technique was first introduced by Jacobi & McKeon (2011) and was refined by Duvvuri & McKeon (2015).

Another way to force the boundary layer is to impose a spatially and temporally varying freestream velocity outside of it. Initially these small-scale velocity modulations inside the boundary layer due to a nearby shear layer were observed by Duffin (2009). Motivated by these observations, in Ranade (2016); Ranade *et al.* (2016) a boundary layer was forced externally by a two-dimensional shear layer formed by the mixing of two parallel streams. The shear layer was mechanically forced and produced regularized large scale vortical disturbances. These large scale vortical disturbances effectively vary the freestream external velocity experienced by the boundary layer and influence the large and small scale dynamics in the boundary layer. The effects of the external forcing on localized turbulence production in the boundary layer were extensively studied using hot wire anemometry techniques (Ranade *et al.*, 2016; Ranade, 2016). It was shown that this external spatio-temporal forcing produces periodic turbulent modulation events in the boundary layer during an accelerating portion of the external flow. These events were found to be phase-locked to the traveling shear layer structures.

Approach

One way to non-intrusively study large-scale structures in boundary layers, as previously suggested by Duffin (2009), is to measure related density distortions via optical methods. Turbulent density fluctuations that are present in the turbulent region change the local speed of light passing through the turbulent region; this phenomenon is known as the aero-optic problem (Wang *et al.*, 2012; Jumper & Gordeyev, 2017). As planar wavefronts propagate through these unsteady density distributions, they become distorted and these distortions can be accurately measured by various wavefront sensors. As the main mechanism of density fluctuations in the canonical boundary layer is the Strong Reynolds Analogy (SRA), these wavefronts are primarily related to the instantaneous velocity field. Thus, they provide important information about the velocity field and the large-scale structures (Gordeyev *et al.*, 2014, 2015*a*; Gordeyev & Smith, 2016; Gordeyev & Juliano, 2017).

Most velocity-measurement techniques, like hot-wires or PIV, provide detailed information about the velocity field either in selected points or along a plane. On the other hand, while integrated in the beam propagation direction, wavefronts provide spatial information about the structures along a plane normal to the beam direction. Consequently, when wavefronts are simultaneously measured with the velocity field, these wavefronts provide additional data about the large-scale structures, like the pressure field inside and streamwise/spanwise statistics of the large-scale structures (Gordeyev *et al.*, 2015*b*; Gordeyev & Smith, 2016; Gordeyev & Juliano, 2017). One of the assumptions of the SRA is negligible pressure fluctuations, so all density fluctuations are presumed to be via adiabatic cooling/heating. Recent studies of canonical boundary layers (Gordeyev & Smith, 2016) have shown that most of the time

the instantaneous version of SRA,

$$CpT'(\vec{x},t) = \overline{U}u'(\vec{x},t) \quad (1)$$

correctly explains the instantaneous aero-optical distortions, *OPD*. Here *OPD* stands for Optical Path Difference and is defined as an integral of the index-of-refraction along the beam propagation, y,

$$OPD(x,z,t) = \int n'(x,y,z,t)dy = K_{GD}\int \rho'(x,y,z,t)dy \quad (2)$$

and K_{GD} is a Gladstone-dale constant. *OPD* is simply the conjugate of a wavefront. Using Eq. (1), the density field can be related to the instantaneous velocity field (Gordeyev *et al.*, 2014),

$$\frac{\rho'(x,y,z,t)}{\rho_\infty} = (\gamma-1)M_\infty^2\frac{\overline{U}(y)u'(x,y,z,t)}{U_\infty^2}. \quad (3)$$

If only statistics of aero-optical distortions are of interest, they can be computed either using Eq. (2) or through the so called "linking-equation" of Sutton (1969),

$$OPD_{rms}^2 = 2K_{GD}^2\int \rho_{rms}^2\Lambda_\rho(y)dy \quad (4)$$

where Λ_ρ is a correlation length in the wall normal direction and subscript *rms* denotes a temporal variance.

Aero-optical distortions provide non-intrusive means of inferring information about the instantaneous density or velocity field; the integration in the definition of *OPD*, Eq. (2), implies that *OPD* is primarily related to large-scale structures. As a final comment, if the pressure fluctuations inside the large-scale structures are not negligible, one can study pressure variations inside these events by comparing velocity fields and corresponding wavefronts (Gordeyev & Smith, 2016).

So, performing optical measurements along with traditional velocity measurements, one can glean additional information about turbulent flows. Inspired by these recent results, a similar approach was taken to study the turbulence amplification phenomenon in the externally-forced boundary layer, mentioned before (Ranade, 2016). As the signal used to force the shear layer was periodic, it provided a convenient way to phase-lock the velocity measurements inside the boundary layer to the external forcing. If the aero-optical measurements of the forced boundary layer were also phase-locked, it would allow for direct comparison of the phase-locked velocity fluctuations and related OPDs during the amplification events.

EXPERIMENTAL SETUP

The compressible two-dimensional shear layer facility in the Hessert Laboratory for Aerospace Research at the University of Notre Dame was used for these experiments, see Figure 1. The facility is an in-draft tunnel comprised of two inlets, one for high speed, $M = 0.6$, or $U_0 = 200$ m/s, flow and one for low, $M = 0.07$, $U_{low} = 24$ m/s, speed flow to form a planar shear layer. Distance between the side walls was 10 cm.

A schematic of the experimental setup can be seen in Figure 2. A splitter plate, separating the two flows, is located 80 mm from the wall, where the boundary layer under study was located. A row of voice coil actuators, mounted on the tip of the splitter plate 430 mm upstream of the measurement location, was used to periodically force the shear layer. The forcing signal sent to the voice-coil actuators was a two-harmonic signal, the fundamental harmonic at 675 Hz and a 10%-amplitude subharmonic at 337.5 Hz. This combination was found by Duffin (2009) to produce a regularized traveling vortical structure outside the boundary layer. An unsteady pressure Kulite sensor was installed on a side wall in the middle of the shear layer to monitor static pressure fluctuations. Extensive unsteady pressure and velocity (using hot wires) phase-locked measurements were conducted by Ranade *et al.* (2016); Ranade (2016) in order to better understand the turbulence production and amplification in the boundary layer under the external excitation. The boundary layer thickness at the measurement station was $\delta = 19.7$ mm, with $Re_\theta = 31{,}000$ and $Re_\tau = 5{,}700$.

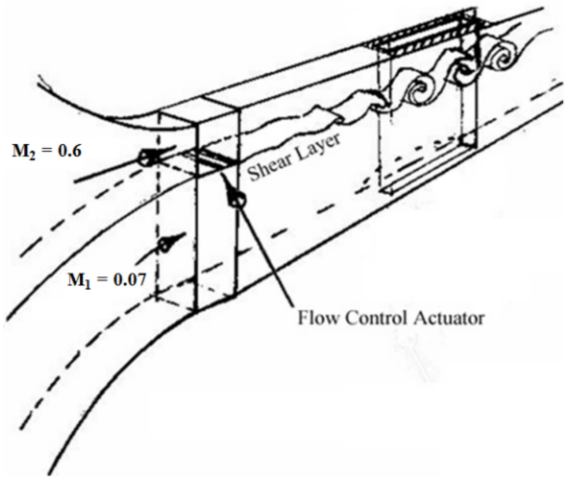

Figure 1. Schematic of compressible share-layer facility.

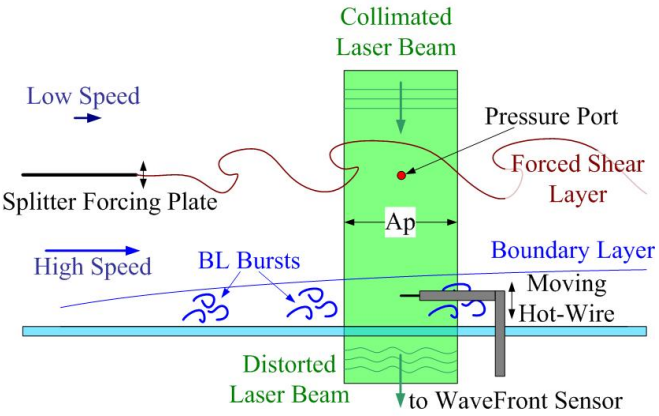

Figure 2. Schematic of the experimental setup.

In our experiment, a collimated laser beam of 250 mm in diameter was sent through the test section in the wall normal direction, see Figure 2. The location of the beam was chosen such that the center of the beam matched the measurement location of the hot-wire velocity data from Ranade *et al.* (2016); Ranade (2016). Wavefronts were collected at 37,125 Hz using a high-speed Wavefront Sensor with spatial resolution of 3.7 mm. The shear layer was forced the same way it was forced for velocity measurements in Ranade *et al.* (2016); Ranade (2016) and the collected wavefronts were phase-locked to the forcing frequency the same manner as the velocity data. In this case, the resulted phase-locked wavefronts can be directly compared to the previously studied phase-locked velocity data.

RESULTS AND DISCUSSION

Figure 3 shows time-averaged the velocity profile, $\overline{U}(y)$, along the wall normal direction at the measurement station. It is comprised of a shear layer velocity profile ($y/\delta = 2-6$) and a boundary

layer on the wall, with a clear uniform region between the shear and the boundary layers. All velocity results in this paper are normalized by the high-speed velocity, U_0, and all high-speed quantities will be denoted with the subscript "0".

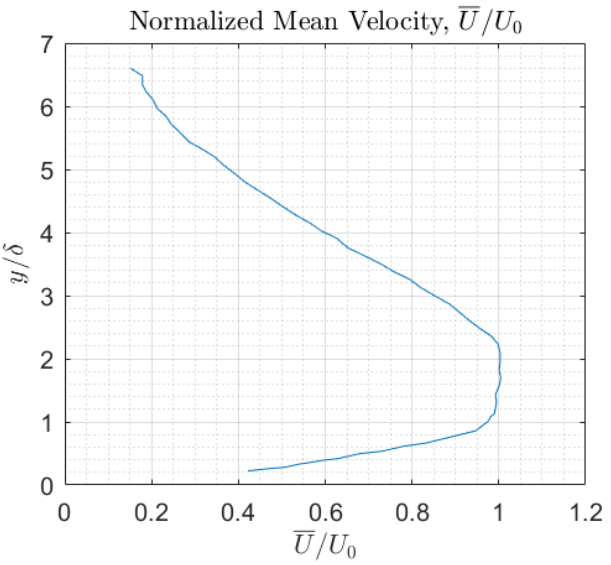

Figure 3. Time-averaged velocity profile at the measurement station, normalized by the high-speed velocity, U_0. The splitter plate is located at $y/\delta = 4.1$

The forced shear layer introduced periodic traveling variations of the velocity and pressure fields outside the boundary layer. These variations convect at a constant speed of approximately $0.5(U_{low} + U_0) = 0.56U_0$. To study phase-locked quantities, ensemble-averaging for various fixed phases was performed, later denoted by a tilde, $\widetilde{f} = \langle f(\phi)\rangle_{\text{Over-All-Ensembles}}$. Figure 4, top, shows the phase-locked velocity and pressure results. Because of the inclusion of the subharmonic into the forcing signal, the studied phase range in this paper will be between 0 and 4π. To better see the phase-locked velocity variations at different phases, the time-averaged velocity profile from Figure 3 was subtracted from the phase-locked velocity results. The relationship between the pressure and velocity signals can clearly be seen. The two signals are approximately π radians out of phase with one another, i.e., when the pressure reaches a minimum inside the shear later structure, the phase-locked velocity throughout the shear layer reaches a maximum and vice versa. These signals effectively represent the varying external boundary condition present on the boundary layer itself. This time varying boundary condition felt by the boundary layer eventually causes an amplification in observed turbulence in the boundary layer.

In the boundary layer, there is only a slight change in the phase of the velocity field, relative to the velocity outside of the boundary layer. The magnitude of the phase-changing velocity is largest in a region of $y/\delta = 0.2 - 0.6$, with values close to 10% of the free-stream velocity, and reaches a maximum value at $y/\delta \approx 0.4$.

Figure 4, center, shows the phase-locked turbulence intensity, reported by Ranade *et al.* (2016); Ranade (2016). Localized inclined regions of the amplified turbulence intensity can be seen near phase values of π and 3π. There is a clear phase variation of the turbulence with increasing wall-normal distance. Near the wall, the turbulence intensity is almost directly in phase with the large-scale external disturbance. Closer to the boundary layer edge, the turbulence tends to be slightly ahead of the large-scale disturbance. The largest phase-locked values of turbulent intensity occurs in a region of $y/\delta \approx 0.3$ and they are approximately in phase with the external velocity variation.

For canonical boundary layers, the maximum turbulence intensity is very near the wall; however, for this externally-forced boundary layer it is shifted away from the wall, to $y/\delta \approx 0.3$. Note from Figure 3, that the mean velocity at this wall-normal location is equal to the convective speed the external disturbances by the shear layer, $0.56U_0$. The matched speeds indicate the existence of a "critical layer" at this location; these "critical layers" were shown to provide the main amplification mechanism in turbulent flows and an important feature in resolvent analysis (McKeon & Sharma, 2010; McKeon *et al.*, 2013).

The boundary layer has elevated levels of turbulence, while the freestream has lower turbulence fluctuations. So, the boundary between the "low" and "high" turbulence can be interpreted as a "edge" of the boundary layer. From Figure 4, center, it can be observed that the boundary layer is the thickest near phases $\pi/2$ and $5\pi/2$, while it is the thinnest at $3\pi/2$ and $7/2\pi$. Interestingly, these locations do not correspond to neither maxima nor minima of the freestream external velocity. Rather, they correlate better with the regions of the external flow deceleration.

Figure 4, bottom, presents the experimental phase-locked temporal variance in aero-optical distortions, OPD_{rms}, in a single point at the same location, where the velocity data were collected. The peaks or maxima in OPD_{rms} are present near $\phi = 3\pi/4$ and $11\pi/4$. They match well to the turbulence amplification related events, seen in Figure 4, center. The peaks in OPD_{rms} are better aligned with the turbulence increase in the outer portion of the boundary layer, $y/\delta > 0.5$, than with the region closer to the wall, where the turbulent intensity is the highest around phases of $5\pi/4$ and $13\pi/4$. It is consistent with the previous notion that large-scale structures are primarily responsible for aero-optical distortions. Additional peaks in OPD_{rms} at $\phi = \pi/4$ and $9\pi/4$ will be discussed later.

The minima in the experimental OPD_{rms} are at $3\pi/2$ and $7\pi/2$ and they do not correlate with the regions of the smallest turbulence fluctuations (at 0 and 2π). Rather, they tend to coincide with the regions where the boundary layer is the thinnest. As OPD_{rms} is an integral quantity, it is expected to be the smallest when integrated through the less-extended region of turbulence.

It is straightforward to derive a phase-locked version of the "linking" equation, Eq. (4), by substituting a phase-locked version of Eq. (3) into Eq. (4),

$$OPD_{rms}(\phi) = \sqrt{2}K_{GD}\left\{\int \rho^2_{rms}(y,\phi)\Lambda_\rho(y)dy\right\}^{1/2} \tag{5a}$$

$$\rho_{rms}(y,\phi) = (\gamma-1)M_0^2\rho_0\frac{\widetilde{U}(y,\phi)\widetilde{u}_{rms}(y,\phi)}{U_0^2} \tag{5b}$$

As mentioned before, the SRA properly predicts the time-averaged levels of OPD_{rms} for canonical boundary layers (Gordeyev *et al.*, 2014, 2015*a*). Using Eqs. (5), SRA-predicted levels of OPD_{rms} were computed using the phase-locked velocity field, Figure 4, top, and the turbulence intensity data, Figure 4, middle. The integration of the SRA-predicted OPD_{rms} was performed inside the boundary layer only, between $y = 0$ and δ. The correlation length of $\Lambda_\rho = 0.12\delta$ was chosen, as suggested in Gordeyev *et al.* (2014).

The values of SRA-predicted OPD_{rms} are plotted as a dotted dashed red line in Figure 4, bottom. While the maximum and minimum values agree well with the experimental results, the locations of the maxima appear to be offset by $\pi/4$. This disagreement between the prediction and the experiment indicate that some assumptions behind the SRA are not valid in the externally-forced boundary

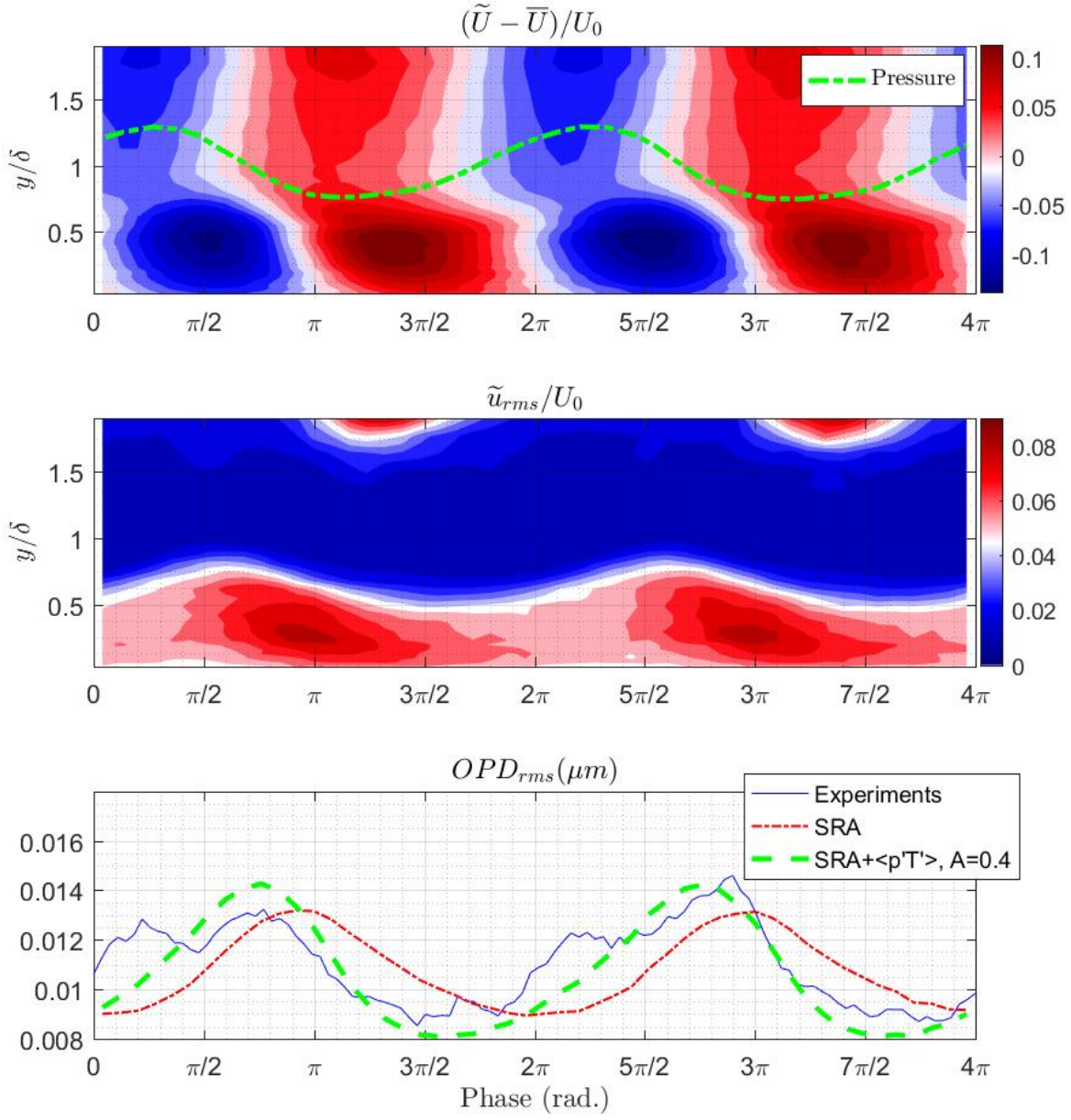

Figure 4. TOP: Phase-locked ensemble-averaged velocity fields. The time-averaged velocity profile from Figure 3 was subtracted for clarity. The phase-locked pressure signal in the middle of the shear layer is indicated by a green dashed line. CENTER: Phase locked turbulence intensity contour plot from Ranade (2016) as a function of phase and wall-normal distance. Turbulent amplification regions inside the boundary layer are seen in red. Turbulence intensity peaks near $y/\delta = 1.8$ are due to the shear layer vortical structures. BOTTOM: Temporal variance of OPD, OPD_{rms}, plotted along with the computed OPD_{rms} using the SRA, Eq. (5) as a dotted dashed line, and using the SRA with additional pressure-related terms, Eq. (5a) + Eq. (9), a dashed green line.

layer. Let us revisit the derivation of the density variation profile, Eq. (5b).

The SRA model assumes that the pressure fluctuations are zero, so the density variation depends only on the temperature variation, which, in turn, is a function of the local value of the velocity, Eq. (1). But the global pressure field, neglected in the SRA, can also affect the density field. A linearized equation of state for a weakly-compressible flow gives $\rho'/\rho_0 = T'/T_0 - p'/P_0$ or, for the ρ_{rms},

$$\frac{\rho_{rms}^2}{\rho_0^2} \approx \frac{T_{rms}^2}{T_0^2} - 2\frac{\langle p'T'\rangle}{T_0 P_0} \tag{6}$$

Here we ignored a higher-order p_{rms}^2 term, as pressure fluctuations are several times smaller than the velocity fluctuations. Streamwise variations in the velocity field in Figure 4, top, will create the pressure variations, and these pressure changes via $\langle p'T'\rangle$-term will result in additional density variations, the second term in Eq. (6), and, consequently, in additional aero-optical effects. Neglecting the viscous terms, a linearized version of the momentum N-S equation gives,

$$\frac{1}{\rho_0}\nabla p' \approx -\partial \mathbf{u}'/\partial t - (\mathbf{u}'\cdot\nabla)\widetilde{\mathbf{U}} - (\widetilde{\mathbf{U}}\cdot\nabla)\mathbf{u}' \tag{7}$$

Small-scale structures have negligible associated pressure variations, as the pressure is primarily affected by the changes in the

velocity field over large scales. Thus, we argue that the contribution of the third term in r.h.s. of Eq. (7) is small, compared to the second term. Finally, we used "thin boundary layer" approximation $\partial/\partial y \approx 0$, and the frozen field assumption, $\partial/\partial t \approx -\overline{U}\partial/\partial x$, to get $\partial p'/\partial x \approx -\rho_0 u'\partial(\widetilde{U}-\overline{U})/\partial x$. Integrating this equation, we get the following estimation of the pressure fluctuations,

$$p' \approx -A\rho_0 u'(\widetilde{U}-\overline{U}) \tag{8}$$

Here A-constant is introduced in attempt to account for the missing information in the wall-normal direction, including a possible effect from the wall-normal velocity component. Substituting Eqs. (8) and (1) into Eq. (6) and performing the phase-locked ensemble averaging we can get a better estimate for the phase-locked variation of the density field,

$$\rho^2_{rms}(y,\phi) = \left[(\gamma-1)\rho_0 M_0^2\right]^2 \frac{\widetilde{u}^2_{rms}(y,\phi)}{U_0^2} \times \left\{ \frac{\widetilde{U}(y,\phi)^2}{U_0^2} - 2A\frac{\gamma}{(\gamma-1)}\frac{\widetilde{U}(y,\phi)\Delta U}{U_0^2} \right\} \tag{9}$$

with $\Delta U \equiv \widetilde{U}(y,\phi) - \overline{U}(y)$. In absence of external forcing (a canonical boundary layer), $\Delta U = 0$, and Eq. (9) is reduced to Eq. (5b).

Different values of A were tried and the levels of OPD_{rms} were calculated, using Eq. (5a) with Eq. (9). Results with $A = 0.4$ are plotted in Figure 4, bottom, as a dashed green line. The agreement with the experiments is much better, as this updated model properly predicts all essential features of the optical distortions, including the locations and the magnitudes of the maxima and the minima.

These results indicate that the pressure-related variations, $\langle p'T'\rangle$, are not negligible inside the externally-forced boundary layer, as suggested by the SRA, and play an important role in the resulted aero-optical distortions. These pressure variations also should be taken into account when modelling the dynamics of these turbulence amplification events in the boundary layer.

It is plausible to assume that the pressure-related effects could also be important, at least locally, in canonical boundary layers where the pressure fluctuations, as suggested by Eq. (8), might be induced by a short-lived large deviation of the local flow from the mean velocity due to the presence of the (very) large-scale structure; some evidence of these pressure-related optical effects were presented and discussed in Gordeyev & Smith (2016). Finally, recent studies of an adverse pressure gradient boundary layer by Schatzman & Thomas (2017) demonstrated that the local flow physics is largely dominated by an inflectional instability which gives rise to an embedded shear layer, with related pressure fluctuations.

The only regions of the visible deviations between the experiments and the predictions with the updated model can be observed between $\phi = 0..\pi/2$ and $\phi = 2\pi..5\pi/2$, where experimental OPD_{rms} is consistently higher than predicted by the updated SRA model. At these phases, the pressure inside the shear layer is the largest, see Figure 4, top, corresponding to the locations between the vortical structures inside the shear layer, called "braids". Inspection of the unsteady pressure signal (not shown) had revealed that the pressure fluctuations were indeed higher in "braid" regions, compared to to the low pressure regions; these elevated pressure fluctuations are responsible for the observed additional increases in OPD_{rms} near $\phi = \pi/4$ and $9\pi/4$.

Another unique feature of wavefront measurements is that the wavefronts are measured at multiple, typically hundreds, points over the aperture. In essence, they provide time-resolved "snapshots" of the field over many spatial points in both the streamwise and the spanwise directions.

Collected wavefronts spanned 250 mm in the streamwise direction and 100 mm in the spanwise direction, or over a $[13\delta \times 5\delta]$ region. As wavefronts mostly convect at a constant speed of approximately $0.5(U_0 + U_{low})$, this streamwise spatial extend corresponds to approximately 4π-range in the phase. If the correlation function were computed over a full streamwise spatial extent, it would average out events during the high-turbulence and low-turbulence events, as well as would include contaminating aero-optical events from the shear layer. So in order to study statistics of the spatial wavefronts during the maxima and the minima of OPD_{rms}, the wavefronts were cropped down to $[4\delta \times 5\delta]$, centered at the hot-wire measurement point.

One way to use this spatial information is to compute the normalized phase-locked spatial correlation function, $\rho(\Delta x, \Delta z; \phi) = R(\Delta x, \Delta z; \phi)/R(0,0;\phi)$, where

$$R(\Delta x, \Delta z; \phi) = \langle OPD(x,z,\phi) OPD(x+\Delta x, z+\Delta z, \phi)\rangle.$$

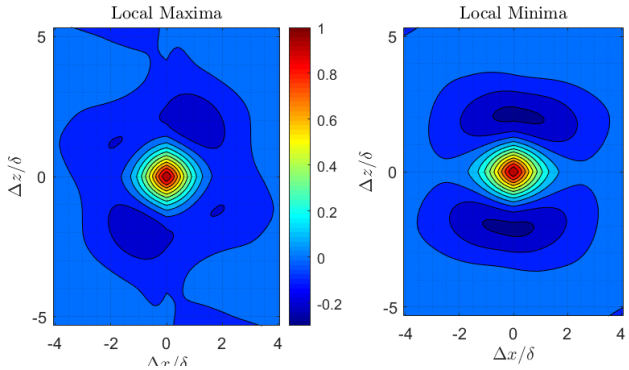

Figure 5. Normalized phase-locked correlation, $\rho(\Delta x, \Delta z; \phi)$ during the local maximum of OPD_{rms}, $\phi = 3\pi/4$ (left), and during the local minimum of OPD_{rms}, $\phi = 3\pi/2$ (right).

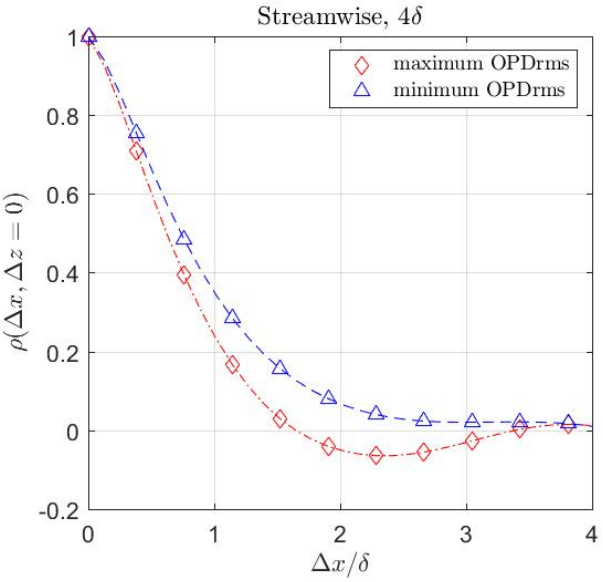

Figure 6. Streamwise wavefront correlation function, $\rho(\Delta x, \Delta z = 0)$

.

Figure 5 shows two-dimensional phase-locked correlations during the maxima and minima of the temporal variance of OPD. Figures 6 and 7 show the same wavefront correlation function as one-dimensional "slices" the in the streamwise, $\rho(\Delta x, \Delta z = 0)$, and in the spanwise directions, $\rho(\Delta x = 0, \Delta z)$, respectively. Now, we

can investigate the spatial extent of the optical structures during the amplified turbulence events.

In Figure 6, the streamwise wavefront correlation during the minima becomes slightly negative at $\Delta x/\delta \approx 2$, while during the minima the streamwise correlation function stays positive for all Δx-separations. This implies that during the turbulence amplification events a stronger, more organized optical structure is formed in the boundary layer. This organization might be related to the presence of the phase-locked global pressure field, as discussed before.

In Figure 7, both curves show the presence of the periodic structure with a typical size of $\Delta z/\delta \approx 2$. However, the trend is the opposite: the optical structure is more organized during low turbulence event, indicated by a smaller negative value of -0.2 at the minimum of ρ, then during the turbulence amplification event, where the minimum value of ρ is larger, about -0.1.

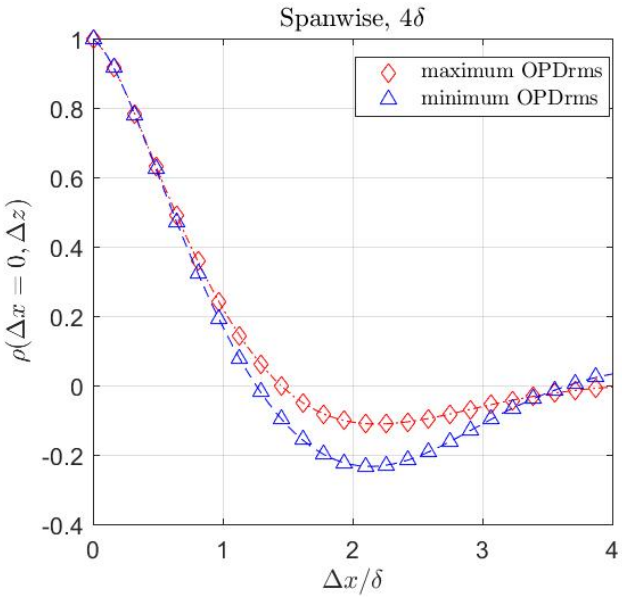

Figure 7. Spanwise wavefront correlation function, $\rho(\Delta x = 0, \Delta z)$

As this information is difficult to get from point-measurements of the velocity field, it demonstrates that the wavefronts provide additional valuable information about the turbulence amplification events. Overall, optical wavefront sensing techniques allow for quantitative, time resolved density-related data in both the spanwise and streamwise directions. This is a distinct advantage of the described optical wavefront sensing method. Also, optical wavefront are functions of the density field only and the density field is very difficult to measure directly by other experimental techniques. Even though the wavefront sensing technique is by nature an integrated measurement, a comparison between the velocity filed and the related wavefronts provide useful information about the topology and dynamics of the large-scale events in the boundary layers.

REFERENCES

Duffin, Daniel A. 2009 Feed-forward adaptive-optic correction of a weakly-compressible high-subsonic shear layer. Ph.D Dissertation, University of Notre Dame.

Duvvuri, Subrahmanyam & McKeon, Beverley J. 2015 Triadic scale interactions in a turbulent boundary layer. *Journal of Fluid Mechanics* **767**.

Gordeyev, Stanislav, Cress, Jacob A., Smith, Adam & Jumper, Eric J. 2015*a* Aero-optical measurements in a subsonic, turbulent boundary layer with non-adiabatic walls. *Physics of Fluids* **27** (4).

Gordeyev, Stanislav & Juliano, Thomas J. 2017 Optical measurements of transitional events in a mach-6 boundary layer. *To appear in AIAA Journal* .

Gordeyev, Stanislav & Smith, Adam 2016 Studies of the large-scale structure in turbulent boundary layers using simultaneous velocity-wavefront measurements. In *46th AIAA Fluid Dynamics Conference*. AIAA-2016-3804.

Gordeyev, Stanislav, Smith, Adam E., Cress, Jacob A. & Jumper, Eric J. 2014 Experimental studies of aero-optical properties of subsonic turbulent boundary layers. *Journal of Fluid Mechanics* **740**, 214–253.

Gordeyev, Stanislav, Smith, Adam E., Saxton-Fox, Theresa & McKeon, Beverley J. 2015*b* Studies of the large-scale structure in adiabatic and moderately-wall-heated subsonic boundary layers. In *9th International Symposium on Turbulence and Shear Flow Phenomena (TSFP-9)*. Paper 7A-3.

Jacobi, I. & McKeon, B. J. 2011 Dynamic roughness perturbation of a turbulent boundary layer. *Journal of Fluid Mechanics* **688**, 258–296.

Jumper, Eric J. & Gordeyev, Stanislav 2017 Physics and measurement of aero-optical effects: Past and present. *Annual Review of Fluid Mechanics* **49**, 419–441.

Kline, S. J., Reynolds, W. C., Schraub, F. A. & Runstadler, P. W. 1967 The structure of turbulent boundary layers. *Journal of Fluid Mechanics* **30** (4), 741–773.

McKeon, B. J. & Sharma, A. S. 2010 A critical-layer framework for turbulent pipe flow. *Journal of Fluid Mechanics* **658**, 336–382.

McKeon, B. J., Sharma, A. S. & Jacobi, I. 2013 Experimental manipulation of wall turbulence: A systems approach. *Physics of Fluids* **25**, 031301.

Ranade, Piyush M. 2016 Turbulence amplitude modulation in an externally forced, high reynolds number boundary layer. Ph.D Dissertation, University of Notre Dame.

Ranade, Piyush M., Duvvuri, Subrahmanyam, McKeon, Beverley J., Gordeyev, Stanislav, Christensen, Kenneth T. & Jumper, Eric J. 2016 Turbulence amplitude modulation in an externally forced, subsonic turbulent boundary layer. In *54th AIAA Aerospace Sciences Meeting*. AIAA Paper 2016-1120.

Schatzman, D.M. & Thomas, F.O. 2017 An experimental investigation of an unsteady adverse pressure gradient turbulent boundary layer: embedded shear layer scaling. *Journal of Fluid Mechanics* **815**, 592–642, doi:10.1017/jfm.2017.65.

Sutton, G. W. 1969 Effect of turbulent fluctuations in an optically active fluid medium. *AIAA Journal* **7** (9), 1737–1743.

Wang, Meng, Mani, Ali & Gordeyev, Stanislav 2012 Physics and computation of aero-optics. *Annual Review of Fluid Mechanics* **44** (1), 299–321, http://dx.doi.org/10.1146/annurev-fluid-120710-101152.